

# PropSAM: A Propagation-Based Model for Segmenting Any 3D Objects in Multi-Modal Medical Images

Zifan Chen<sup>1\*</sup>, Xinyu Nan<sup>1\*</sup>, Jiazheng Li<sup>2\*</sup>, Jie Zhao<sup>3</sup>, Haifeng Li<sup>4</sup>, Zilin Lin<sup>1</sup>, Haoshen Li<sup>1</sup>, Heyun Chen<sup>1</sup>, Yiting Liu<sup>2</sup>, Bin Dong<sup>4,5,6✉</sup>, Li Zhang<sup>1,4✉</sup>, and Lei Tang<sup>2✉</sup>

<sup>1</sup>Center for Data Science, Peking University, Beijing, China

<sup>2</sup>Department of Radiology, Key Laboratory of Carcinogenesis and Translational Research (Ministry of Education), Peking University Cancer Hospital and Institute, Beijing, China

<sup>3</sup>National Engineering Laboratory for Big Data Analysis and Applications, Peking University, Beijing, China

<sup>4</sup>National Biomedical Imaging Center, Peking University, Beijing, China

<sup>5</sup>Beijing International Center for Mathematical Research (BICMR), Peking University, Beijing, China

<sup>6</sup>Center for Machine Learning Research, Peking University, Beijing, China

August 27, 2024

\*These authors contributed equally: Zifan Chen, Xinyu Nan, Jiazheng Li

## ✉Correspondence to:

- Prof. Bin Dong, Beijing International Center for Mathematical Research (BICMR) & Center for Machine Learning Research, Peking University & National Biomedical Imaging Center, Peking University, Haidian District, Beijing, 100080, China, dongbin@math.pku.edu.cn
- Dr. Li Zhang, Center for Data Science & National Biomedical Imaging Center, Peking University, Haidian District, Beijing, 100080, China, zhangli\_pku@pku.edu.cn
- Prof. Lei Tang, Department of Radiology, Key Laboratory of Carcinogenesis and Translational Research (Ministry of Education), Peking University Cancer Hospital and Institute, Haidian District, Beijing, 100142, China, tangl@bjcancer.org

# Abstract

**Background:** Volumetric segmentation is pivotal for medical imaging applications but is often hindered by the extensive manual annotations and model training specific to each medical scenario. Additionally, current general segmentation models underperform and suffer inefficiencies due to their architectural and inferential strategies. There is an urgent need in clinical practice for a segmentation model that is both high-performing and efficient for segmenting any 3D object across various modalities in medical images.

**Methods:** We introduce PropSAM, a propagation-based segmentation model that leverages the continuous flow of information within 3D medical structures. PropSAM combines a CNN-based UNet architecture for intra-slice information processing with a Transformer-based attention module to facilitate inter-slice propagation. This methodology is designed to enhance segmentation effectiveness across various imaging modalities by focusing on structural and semantic continuities rather than isolating specific objects. Built upon this innovative framework, PropSAM is engineered to support a one-view prompt, such as a 2D bounding box or a 2D sketch mask, differentiating it from the conventional two-view prompts typically used.

**Results:** PropSAM demonstrated superior performance on 44 diverse medical datasets, notable improving the dice similarity coefficient (DSC) for hundreds of segmentation object types and multiple medical imaging modalities. Compared to popular models like MedSAM and SegVol, PropSAM achieved an average DSC improvement of over 18.1%, while maintaining stable predictions despite prompt deviation (one-way ANOVA test,  $P \geq 0.5985$ ) and varying propagation configurations (one-way ANOVA test,  $P \geq 0.6131$ ). Due to its efficient architecture and inference strategy, PropSAM exhibited significantly faster inference speeds (Wilcoxon rank-sum test,  $P < 0.001$ ) than existing models. The one-view prompt used by PropSAM also enhanced human prompt efficiency, reducing interaction time by about 37.8% compared to the two-view prompts required by existing methods. Moreover, thanks to its generalized learning focus on structural or semantic propagation relationships between slices, PropSAM displayed robust performance on unseen objects. It demonstrated a notable advantage in handling irregular and complex objects, exhibiting a linear relationship where DSC improvements are negatively correlated ( $r < -0.1249$ ) with the degree of object irregularity. The source code and supplementary materials are available at Github<sup>1</sup>.

**Conclusions:** PropSAM represents a significant advancement in medical image segmentation, offering a tool that is both generalizable and versatile, with an efficient, user-friendly design. Its potential to quickly adapt to new tasks with minimal re-training underscores its promise for clinical applications, potentially paving the way for more automated and reliable medical imaging analyses.

**Key words:** Deep learning, segment any 3D objects, multiple modalities, medical images, volumetric segmentation, propagation-based model

---

<sup>1</sup><https://github.com/czifan/PropSAM>



# 1 Introduction

Volumetric segmentation is an essential task in the analysis of medical imaging [1], which entails the identification and delineation of regions of interest (ROIs) in various objects such as organs, lesions, and tissues within three-dimensional (3D) medical images. Accurately segmenting these objects across various medical imaging modalities—including computed tomography (CT), magnetic resonance imaging (MRI), positron emission tomography-computed tomography (PET-CT), and micro-computed tomography (micro-CT)—is crucial for a multitude of clinical applications. These include disease diagnosis [2, 3, 4], surgical and treatment planning [5, 6], monitoring disease progression [7, 8, 9], and therapy optimization [10, 11]. In most current clinical scenarios [12, 9, 8], manual segmentation within 3D medical images remains the predominant method for delineating anatomical structures and pathological areas. This process is not only time-consuming and labor-intensive but also requires precise segmentation across a diverse objects and imaging modalities [13]. Consequently, there is a pressing need to develop semi-automatic or fully automatic segmentation algorithms capable of handling any medical imaging modality and object. Such advancements are expected to greatly decrease the time and labor involved for segmentation tasks, while also improving the consistency of the delineations [14, 15].

To address these challenges, over the past decade, deep learning-based models have shown great promise in medical image segmentation, owing to their capacity to learn complex image features and achieve precise segmentation across a variety of tasks [16, 1, 17]. However, these successful models are often specifically designed for certain segmentation challenges, a necessity driven by the distinctive demands of various medical imaging modalities and the intricate anatomy of the target objects. Typically, these task-specific models require the assembly of large, meticulously annotated datasets for each new task, where medical experts carefully delineate the ROI for each specific object and modality [18, 19, 20, 21]. While these models frequently deliver high accuracy and robust performance within their designated settings, their reliance on extensive annotated datasets constrains their adaptability and scalability. For every new object or modality, a similar process must be repeated: data collection, manual annotation by medical experts, and model training [1], which is not only resource-intensive but also impractical for addressing emergent medical scenarios or rare pathologies. The considerable cost associated with data annotation and the scarcity of expert annotations further compound these challenges, hindering the broad deployment of these models across diverse clinical environments. Consequently, there is an urgent need for more generalized models that can overcome these limitations, offering the flexibility and rapid adaptability to new tasks without the necessity for repetitive, extensive training on narrowly defined datasets [22].

Recently, the concept of foundation models has gained prominence in the field of natural image processing, where models like the segment anything model (SAM) [23, 24] have demonstrated remarkable generalization capabilities across diverse tasks, thanks to training on vast datasets. The SAM model, trained on extensive and varied image sets, enables precise segmentation with minimal user prompts such as points, bounding boxes, and masks, effectively segmenting any object within an image. Inspired by this success, researchers have begun adapting these versatile frameworks to the medical imaging domain through two primary types of models [13, 25, 26, 27, 28, 29, 30, 31, 32, 33, 34]. The type I model (Figure 1b), often exemplified by MedSAM [13, 35], directly applies the SAM approach to various two-dimensional (2D) medical images. By

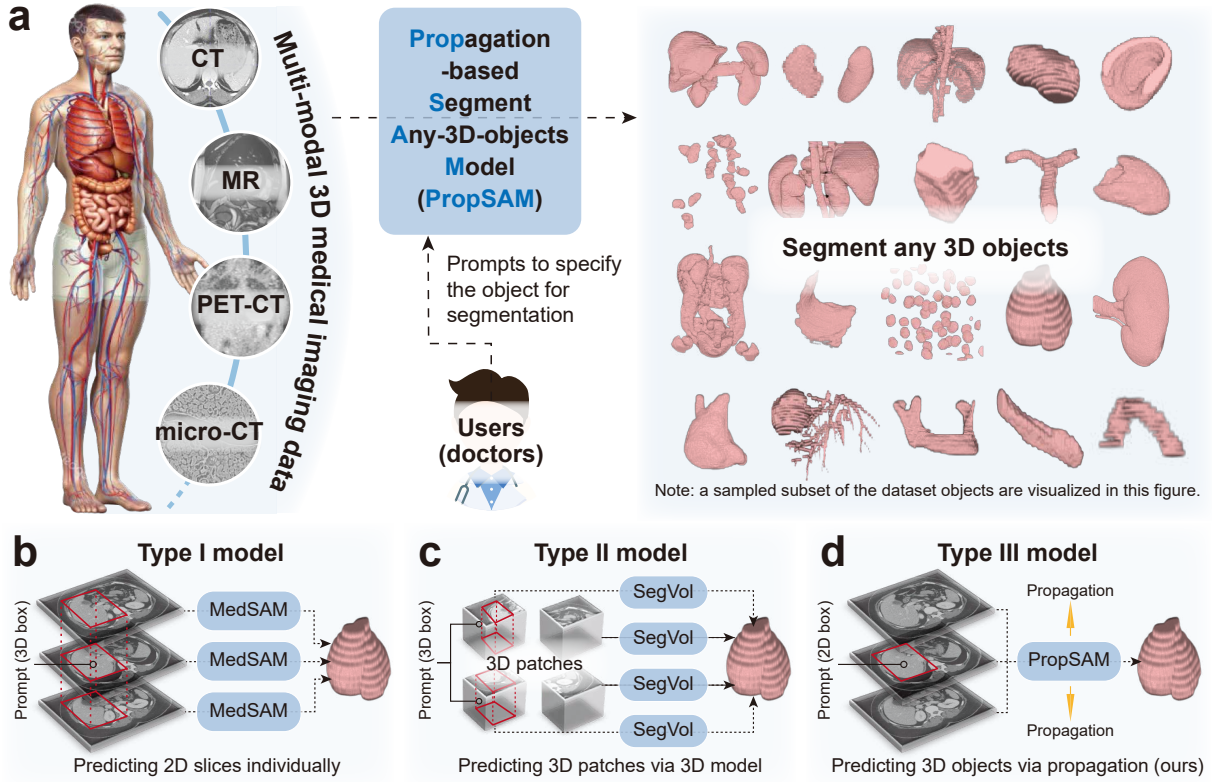


**Figure 1: PropSAM is designed for segmenting any 3D objects within various multi-modal 3D medical imaging data.** **a** PropSAM receives any 3D medical imaging data as input, with users (typically doctors) specifying the target objects for segmentation through prompts. This enables precise and efficient volumetric segmentation of diverse 3D objects, thereby aiding users in enhancing the efficiency of medical analysis and diagnostics. **b** Type I model: receives a 3D box prompt, predicts each 2D slice using a 2D model, and merges these 2D outcomes into a consolidated 3D prediction. **c** Type II model: receives a 3D box prompt, predicts each 3D patch using a 3D model, and integrates these patch results into a comprehensive 3D prediction result. **d** Type III model (ours): receives a 2D box or mask prompt, employs a propagation model to disseminate prompt knowledge throughout across the entire 3D space, resulting in a unified 3D prediction.

training on a comprehensive collection of medical images, MedSAM can perform accurate object segmentation within 2D medical images based on simple user-provided 2D prompts. While MedSAM shows promise in adapting the SAM technology for medical use, it struggles with the complexities of 3D medical imaging. Its lack of consideration for the continuity between adjacent slices in 3D image stacks results in significant challenges in achieving coherent volumetric segmentation. This limitation necessitates more complex user interactions, such as multiple prompts across different anatomical planes or dense annotations on each slice, to achieve satisfactory segmentation results. Recognizing these gaps, further research has led to the proposal of volumetric segmentation models (type II model, Figure 1c), like SegVol [25], which aim to extend the SAM principles to 3D spaces. Although initial efforts have demonstrated potential in segmenting specific sets of 3D medical objects, the architectural design of these models introduces a massive number of parameters, making it difficult to fully unleash their generalization capabilities on limited 3D medical annotated datasets. Additionally, the substantial computational requirements

and relatively complex interaction costs pose challenges for their application in clinical settings.

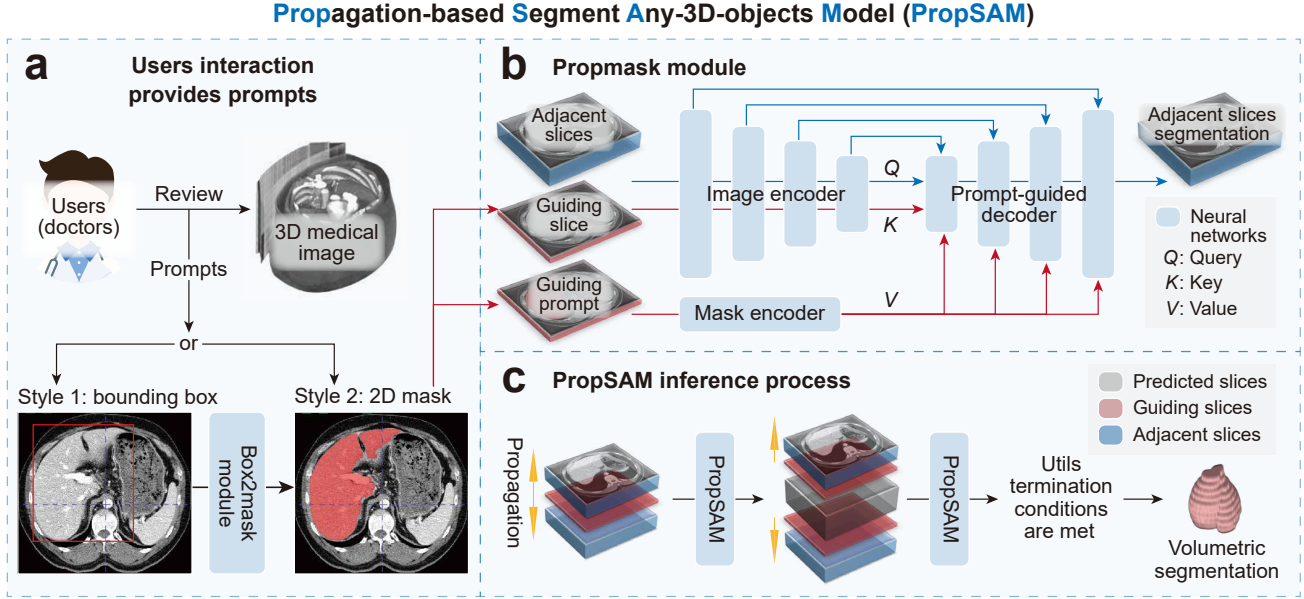


**Figure 2: Workflow and inference process of the propagation-based segment any 3D objects model (PropSAM).** **a** User interaction: users upload a 3D medical image and specify the segmentation target using either a bounding box (style 1), in accordance with response evaluation criteria in solid tumors (RECIST) guidelines, or a 2D mask applied to the largest slice of the target object (style 2). A bounding box is transformed into a 2D mask by the Box2Mask module for standardized processing in the PropMask module. **b** PropMask module: this module conducts volumetric segmentation by propagating information between slices. It begins with the 2D mask and its corresponding image slice (the guiding prompt and slice). Adjacent slices are the targets for segmentation. Image features ( $K$  and  $Q$ ) are extracted from the guiding and adjacent slices, respectively, using a shared image encoder. The guiding prompt is converted into multi-scale features ( $V$ ) through a mask encoder. These features, along with skip connection features from adjacent slices, are assimilated in a prompt-guided decoder to facilitate volumetric segmentation, leveraging the propagation of prompt content across slices. **c** PropSAM inference: the user provides a guiding slice and prompt. PropSAM then propagates the prompt information bidirectionally across slices (yellow arrows). This propagation continues until the boundaries of the 3D image are reached or there is no further content to predict, achieving precise volumetric segmentation.

Given the challenges associated with type I and type II models, we propose addressing these issues by modeling the propagation relationships between slices in 3D medical images, which we refer to as Type III models (Figure 1d). Specifically, we introduce PropSAM, an efficient framework that enhances volumetric segmentation performance via propagation information for any 3D objects within medical images across multiple modalities (Figure 1a). PropSAM achieves this by incorporating a bounding-box to mask module (Box2Mask), trained with over ten million medical images to enable its ability to respond to bounding-box-style prompts, and a propagation module (PropMask), trained with more than one million propagation tasks to understand the propagation relationship between slices in 3D medical images. Within PropSAM, we employ convolutional neural networks (CNN) to design local segmentation components, including the Box2Mask module and the segmentation part of the PropMask module. Additionally, a Transformer-based attention approach models the information propagation relation-

ship between slices. This design renders PropSAM more efficient than other purely Transformer models (e.g., MedSAM and SegVol), resulting in fewer parameters and computations, and faster inference. Additionally, the learning focus of PropSAM is on the propagation of structural or semantic relationships between slices, unlike existing methods that learn from prompts for a lot of specific objects. This approach enables the creation of more numerous and universally applicable learning tasks. We have rigorously evaluated PropSAM through comprehensive experiments on 44 medical datasets, covering a variety of segmentation objects and medical imaging modalities. Experimental results demonstrate that PropSAM consistently outperforms the state-of-the-art (SOTA) segmentation foundation models with greater efficiency. Moreover, PropSAM exhibits robustness with unseen objects and maintains stability across deviated user prompts and different parameter configurations. Furthermore, fine-tuning PropSAM with a small amount of annotated data enables it to quickly transform into a powerful expert model for the novel object type, notably surpassing proprietary models that are trained from scratch on those limited annotated datasets. These results underscore the potential of PropSAM as a new paradigm for versatile volumetric medical image segmentation.

## 2 Results

### 2.1 PropSAM: a propagation-based model for segmenting any 3D objects across multiple medical imaging modalities

The need for an effective volumetric segmentation model in medical imaging is paramount, typically initiated by a user interactive prompt that guides the workflow. Existing models can be categorized into type I and type II models, as illustrated in Figure 1b–c. While these models have demonstrated commendable performance in many scenarios, they possess inherent limitations. Type I models fail to fully address the 3D complexities of medical imaging, whereas type II models, although promising for volumetric analysis, still confront challenges related to computational efficiency and a heavy reliance on 3D annotations to fully leverage model capabilities. In contrast, the inherent continuity of information in 3D medical structures offers an opportunity to exploit 2D models to learn inter-slice propagation relationships, balancing the model’s performance with computational efficiency. Based on this insight, we proposed PropSAM, a propagation-based segmentation model for any 3D objects, also referred to as the type III model in Figure 1d. PropSAM focuses on learning the propagation of information across 2D slices in 3D medical images rather than on specific segmentation objects. This approach not only broadens the model’s general learning tasks but also enhances its general segmentation capabilities. It effectively disseminates knowledge based on the user’s prompt on a slice, achieving efficient and precise 3D segmentation.

As depicted in Figure 2, the workflow of PropSAM starts with a physician reviewing a 3D medical image and providing prompts within a slice for the target objects. PropSAM supports two styles of prompts: bounding boxes and sketch-based masks (refer to Figure 2a, Supplementary Text S1.1, and Supplementary Figure S2). When a bounding box is used, the Box2Mask module executes a foreground segmentation within the box, standardizing the input prompt format as sketch-based masks for subsequent modules. Within PropSAM, the slice annotated by the physician is termed the ‘guiding slice,’ and the corresponding prompt is known as the ‘guiding prompt.’ The PropMask module then plays a crucial role in utilizing

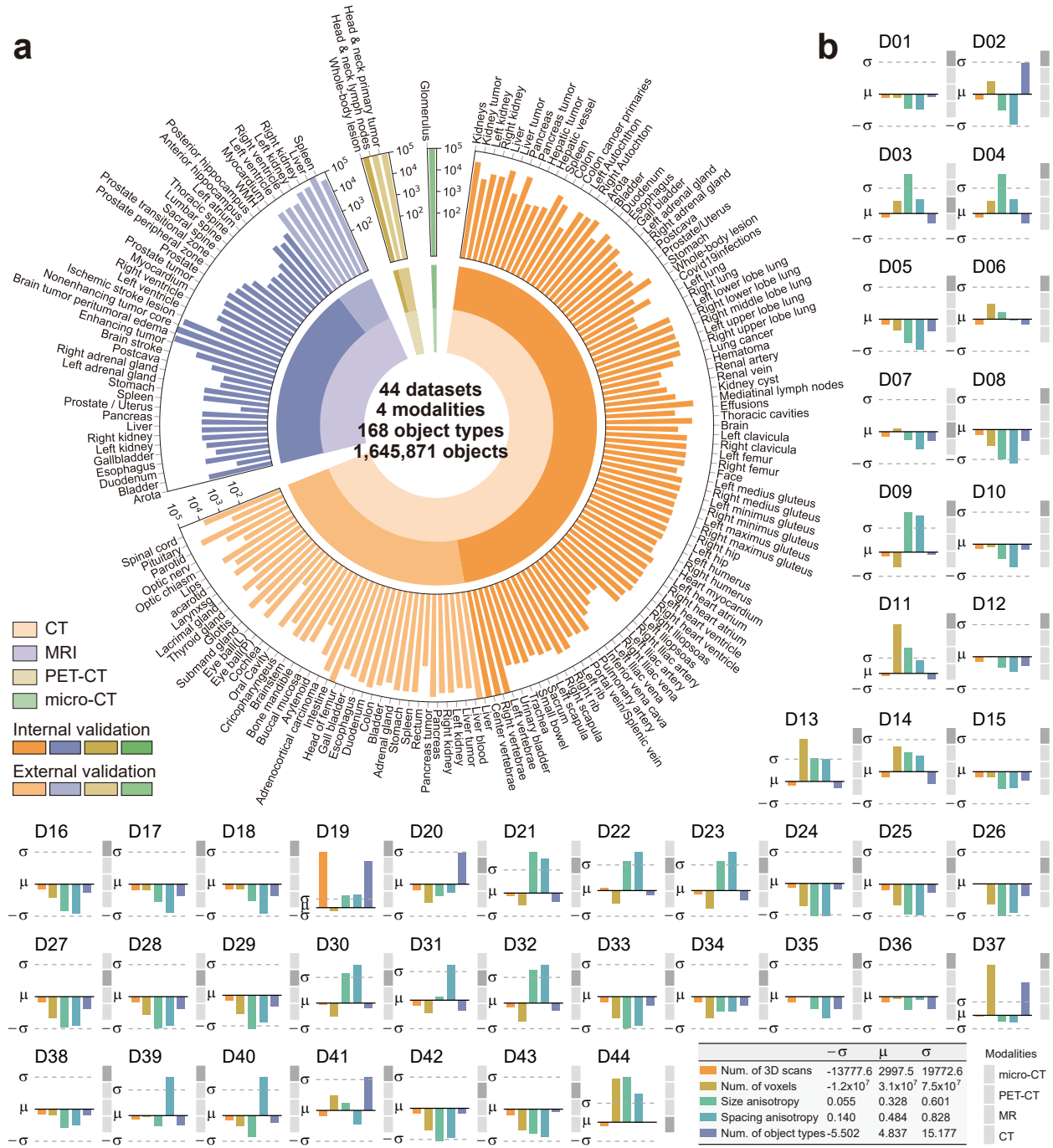


**Figure 3: Data characteristic across various datasets.** **a** A circular barplot illustrates the range of data modalities and validation splits across multiple datasets. The innermost ring uses distinct colors to represent different medical imaging modalities (red for CT; blue for MR; yellow for PET-CT; green for micro-CT). The second ring differentiates between internal and external datasets, with darker shades indicating internal datasets and lighter shades representing external datasets. The outermost layer displays a bar chart that showcases the distribution of segmented object types across the datasets, with quantities log-scaled for optimal visualization. **b** Data fingerprints exhibit the key properties of the 44 datasets used in this study (displayed with z-score normalization over all datasets on a scale of one standard deviation around the mean). see Supplementary Tables S1–S4 for details.

the guiding prompt to segment adjacent slices of the same object (Figure 2b). Initially, the guiding slice and adjacent slices are processed through a shared image encoder to extract image features, forming  $K$  and  $Q$ , respectively. Concurrently, the guiding prompt is transformed via a mask encoder into prompt-guided multi-scale features, termed  $V$ . These features, along with multi-scale features extracted from adjacent slices (as skip connection features), are then combined in a prompt-guided decoder to predict volumetric segmentation. During this process, the PropMask module leverages the information propagation relationships between the guiding slice and adjacent slices to transfer the content of the guiding prompt to the adjacent slices, achieving effective volumetric segmentation. During inference, PropSAM initially employs the physician’s prompt for a preliminary round of segmentation. Subsequent rounds utilize the most marginal slices from previous predictions as new guiding slices, enabling the propagation of the segmentation task through adjacent slices. This process continues iteratively until either the boundary of the 3D medical image is reached or PropSAM has no further content to predict.

## 2.2 Data characteristic and preprocessing

In this study, we compiled 44 3D medical image datasets (Supplementary Table S1), consisting of 43 publicly available datasets and one micro-CT dataset from our clinical practice. These datasets encompass a range of medical imaging modalities, including CT, MRI, PET-CT, and micro-CT, covering 168 different target object types and totaling 1,645,871 3D objects for experimental analysis (see Figure 3a). The diversity of these 44 datasets is categorized across five dimensions (Supplementary Table S4): number of 3D scans, number of voxels, size anisotropy, spacing anisotropy, and variety of object types. This multidimensional diversity is essential for a comprehensive evaluation of PropSAM, as illustrated in Figure 3b. Size anisotropy is defined, following nnUNet [1], as the ratio of the smallest to the largest size in 3D scans, while spacing anisotropy is calculated as the ratio of the smallest to the largest spacing in 3D scans. In alignment with the protocol established in MedSAM [13], we partitioned these datasets into 34 internal datasets (D01–D34) for training and validation, and ten external datasets (D35–D44) for independent testing (Supplementary Tables S2–S3).

As mentioned in the preceding Section 2.1, PropSAM comprises two main modules: the Box2Mask and PropMask modules. For training and evaluating the Box2Mask module, a 2D architecture model (detailed further in Sections 4.1–4.2), we processed 3D images and their 3D annotations through three steps: 1) simulating bounding boxes based on 3D masks to extract ROI images; 2) normalizing these ROI images; 3) applying random data augmentation to enhance the training data (details in Supplementary Text S1.3.2). Following this preprocessing, we obtained a total of 19,344,368 samples (2D medical image-mask pairs), comprising 14,974,620 training samples, 3,782,206 interval validation samples, and 587,542 external validation samples. Additionally, for training and evaluating the PropMask module, a 2D architecture model that receives both guiding slice and prompt and adjacent slices as inputs, we further preprocessed 3D images with their 3D annotations as follows: 1) determining the cropped size to extract both the guiding and adjacent slices, thereby constructing ROI tasks; 2) normalizing these ROI tasks; 3) employing random data augmentation to enhance the training of these ROI tasks (further details in Supplementary Text S1.4.2). Following these preprocessing steps, we amassed a total of 1,345,871 tasks (a guiding slice, a guiding prompt, and several adjacent slices), with 1,020,576 training tasks, 258,889 interval validation tasks, and

66,406 external validation tasks.

### 2.3 PropSAM exceeds the segmentation performance of existing models

We evaluated two version of PropSAM, PropSAM-2DBox which accepts bounding-box-style (style 1) prompts, and PropSAM-2DMask which receives mask-style (style 2) prompts, against two popular existing models, MedSAM and SegVol, on both internal and external datasets. Unlike PropSAM-2DBox, which requires only a single-view prompt such as a 2D bounding box, both MedSAM and SegVol necessitate two-view prompts (typically one bounding box on the axial plane and another on the orthogonal plane) within volumetric medical images. These two-view prompts form the tightest possible 3D bounding boxes of the segmentation targets, restricting the inference to the given slice area (Supplementary Figure S2). Moreover, MedSAM, which is originally designed for 2D medical image segmentation, necessitates processing each 2D medical slice containing the segmentation targets individually. The results from these segmentations are then stacked to form a volumetric final 3D segmentation, following guidance from its official Github <sup>2</sup>. We refer to this process as 'slice-by-slice prediction'. In contrast, SegVol directly segments volumetric medical images and employs a 'zoom-out-zoom-in' strategy using resized global image and cropped patches as inputs to balance the acquisition of both global and local image features. We refer to this process as 'patch-by-patch prediction'.

As illustrated in Figure 4a, our two proposed PropSAMs both exhibit superior segmentation performance (Supplementary Table S5), evaluated by the dice similarity coefficient (DSC), across various experimental datasets and achieve DSCs of 0.95 or 0.95+ on several segmentation objects (e.g. DSC=0.963 for livers, DSC=0.950 for kidneys, and DSC=0.950 for pancreas). Specifically, PropSAM-2DBox and PropSAM-2DMask both achieved higher DSCs on 31 of the 34 internal datasets and all ten external datasets compared to MedSAM and SegVol. Overall, PropSAM-2DBox achieves an average DSC that is 19.7% higher than MedSAM and 18.1% higher than SegVol across all datasets. Similarly, PropSAM-2DMask demonstrates an average DSC that is 25.1% higher than MedSAM and 23.6% higher than SegVol. These results indicates the proposed PropSAMs' robust performance, while demonstrating outstanding performance on external validation datasets. Furthermore, we observed that MedSAM does not demonstrate superior performance on any 3D segmentation tasks due to its 'slice-by-slice prediction'. Besides, SegVol, while showing good performance on organ-related segmentation objects (e.g. DSC=0.941 for livers, DSC=0.912 for kidneys, and DSC=0.842 for pancreas), exhibits a notable decrease in performance on lesion-related or tissue-related segmentation objects (e.g. DSC=0.189 for whole-body lesions, DSC=0.001 for white matter hyperintensities, and DSC=0.080 for glomeruli). These limitations of SegVol stem from the general challenges of 3D segmentation models in limited medical image data, and the 'patch-by-patch prediction' may cause fine information loss and discontinuity, posing challenges in predicting lesions with rare annotations and variable shapes. In contrast, both PropSAM-2DBox and PropSAM-2DMask can accurately segment organ-related, lesion-related and tissue-related segmentation objects. For example, their DSCs are 0.669 and 0.755 for whole-body lesion, 0.443 and 0.569 for white matter hyperintensities, and 0.769 and 0.874 for glomeruli. This indicates the exceptional generalization capabilities of PropSAM, stemming from its ability to learn

---

<sup>2</sup><https://github.com/bowang-lab/MedSAM>



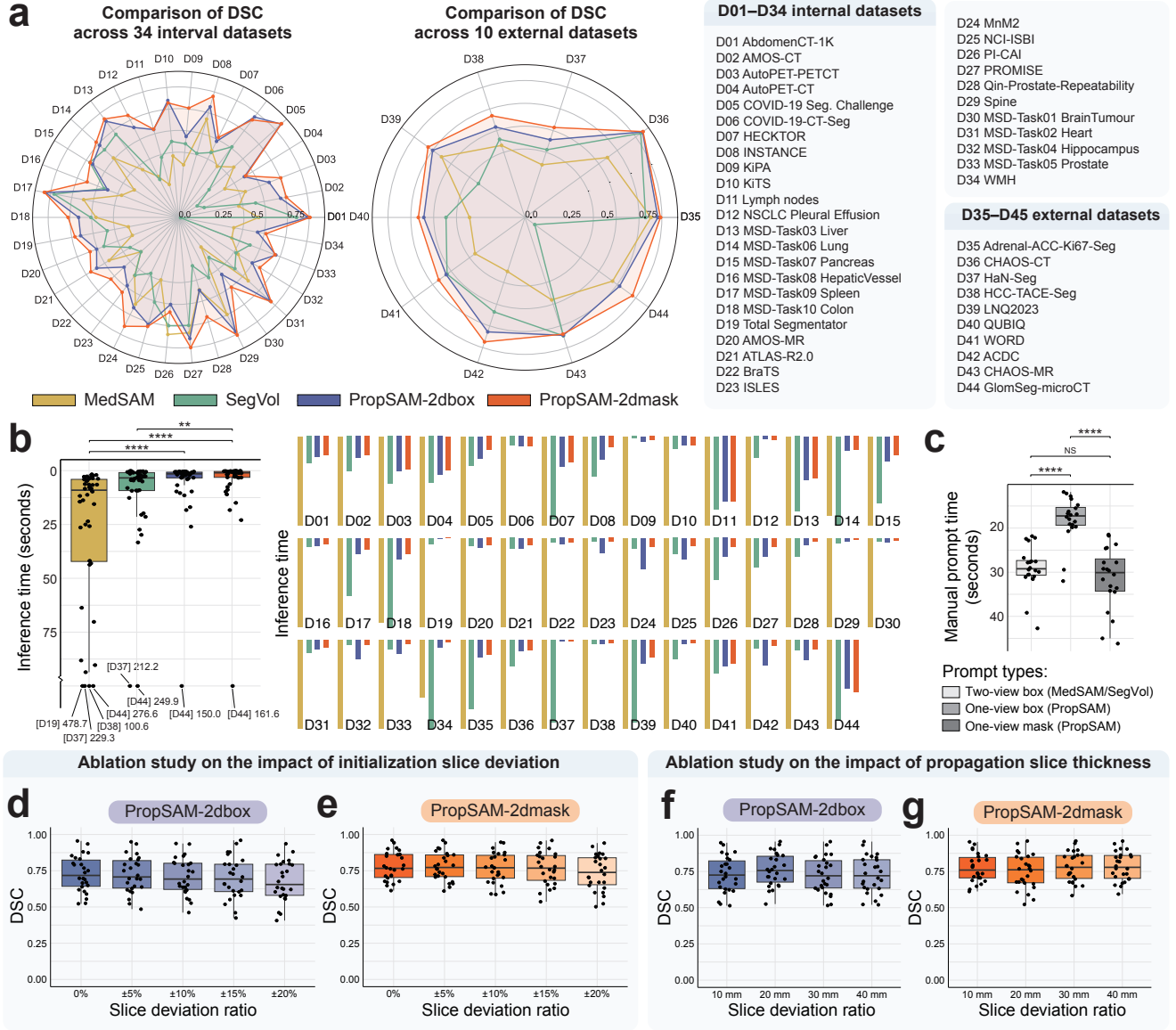


**Figure 4: Quantitative analysis of PropSAM across various datasets.** **a** Radar chart comparisons of dice similarity coefficient (DSC) among four segmentation models—MedSAM (yellow), SegVol (green), PropSAM-2DBox (blue), and PropSAM-2DMask (red)—across internal and external datasets. Each radial axis represents one of the 44 datasets used (D1–D44), with the DSC values ranging from 0.0 to 1.0, moving from the center outward. **b** Comparison of inference times (seconds). The left side features a box plot illustrating the distribution of inference times for the four models across 44 datasets. The right side visualizes a comparative analysis of the inference times for each model across these datasets, where the vertical axis represents inference time, and shorter bars indicate faster inference speeds. **c** Comparison of manual prompt times (seconds). A box plot depicts the distribution of interactive prompt times for three distinct prompt types. Light grey represents the commonly used two-view box prompt (MedSAM and SegVol), medium grey denotes the one-view box prompt of PropSAM, and dark grey signifies the one-view mask prompt of PropSAM. The vertical axis indicates the prompt times. **d–e** Ablation study on the impact of initialization slice deviation. Blue and red colors represent the PropSAM-2dbox and PropSAM-2dmask models, respectively. The box plots show the distribution of DSCs plotted against initialization slice deviation from the RECIST-annotated maximum slice, with deviations of 0% (no deviation),  $\pm 5\%$ ,  $\pm 10\%$ ,  $\pm 15\%$ , and  $\pm 20\%$ . **f–g** Ablation study on the impact of propagation slice thickness. The box plots display the distribution of DSCs plotted against propagation thickness of 10 mm, 20 mm, 30 mm, and 40 mm.



generalized tasks (the propagation of information between slices rather than special objects). These quantitative performance analysis underscore PropSAM’s efficacy in accurately segmenting arbitrary 3D objects across a variety of medical imaging modalities and its potential for clinical applications.

## 2.4 PropSAM demonstrates superior inference and interaction efficiency compared to existing models

We conducted a comprehensive evaluation of the inference times of PropSAMs, MedSAM and SegVol across all datasets. As illustrated in Figure 4b, MedSAM exhibits the slowest inference speeds (the longest inference times), while SegVol shows a speed improvement over MedSAM. However, our proposed PropSAMs, in both the 2DBox and 2DMask versions, consistently achieve the fastest inference speeds (the least inference times). The right side of Figure 4b visually details the specific inference time comparisons across the 44 datasets, with PropSAMs outperforming in nearly all cases (Supplementary Tables S6–S7).

The superior inference speed of PropSAMs can primarily be attributed to two factors: model structure design and inference strategy design. Existing models are generally based directly or largely on the successful SAM models in natural imaging, which employ purely Transformer-based architectures adept at modeling long-distance relationships. However, we observed that in medical images, particularly in segmentation tasks, local information is equally important and contains many anatomical structures and details necessary for accurate segmentation. Long-distance relationships generally exist between different slices of the same anatomical object. Therefore, our PropSAM utilizes a CNN-based architecture, similar to UNet [16], for precise location segmentation while leveraging the attention mechanism in Transformer architectures [36] to model information propagation between slices. This approach not only allows PropSAM to utilize architectures that have proven successful in medical segmentation [16, 1] but also reduces the model’s parameter count (a total of 32.48 M parameters and 53.1 M parameters when combined with Box2Mask module for supporting bounding-box prompts). In terms of inference strategy, MedSAM, a type I model, predicts each slice individually with a complex Transformer model in response to a prompt, requiring extensive computational resources (Figure 1b). SegVol, a type II model, adopts a inference process similar to the 3D-nnUNet model, predicting individual patches with dense overlapping strides that are later merged. This not only increases the computational cost due to the 3D model’s inherent complexity but also leads to increased prediction overhead and potential artifacts during patch merging due to the small stride in sliding window patch prediction (Figure 1c). In contrast, PropSAM, belonging to type III models, requires only the parameter count and computational load of a 2D model and allows bidirectional parallel inference without the need for overlapping window slides (Figure 1d). Consequently, PropSAM offers a more efficient pipeline for segmenting any 3D objects, making it notable more efficient than existing models.

Furthermore, we explored the interaction efficiency of different models. Both MedSAM and SegVol require two-view prompts, whereas PropSAM-2DBox only necessitates interaction in one view. In our extracted test subset (see Supplementary Text S2 for more experimental details), an experienced radiologist interacted with different datasets and objects using the various interaction prompts. We recorded the time taken for each interaction and compared the different prompt types. As demonstrated in Figure 4c, the one-view box prompt of PropSAM took significantly less times than the most common two-

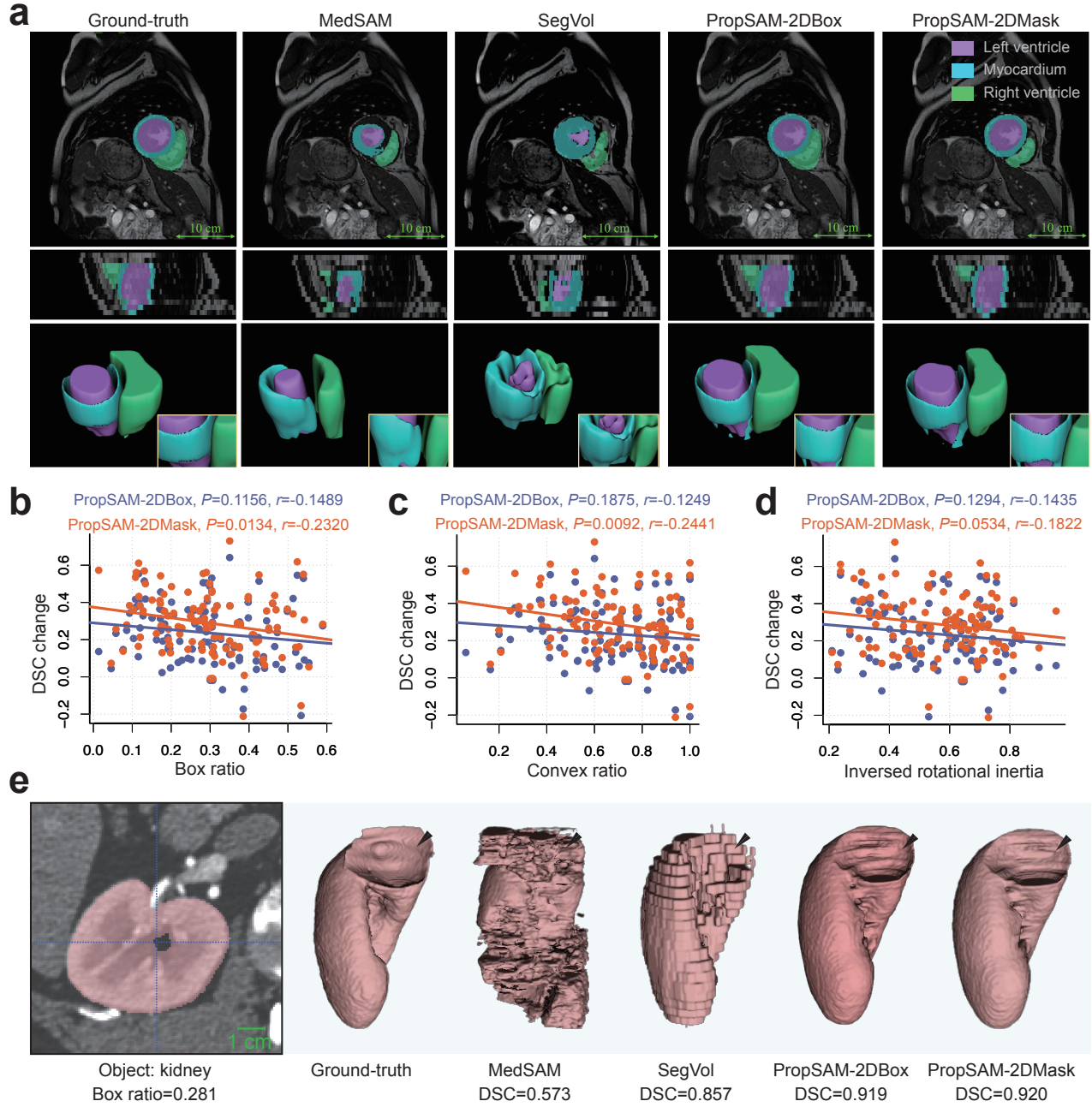


**Figure 5: Qualitative analysis and the relationship between object shape and performance.** **a** Comparison of segmentation results across various models. From left to right, the columns represent ground truth, MedSAM, SegVol, PropSAM-2DBox, and PropSAM-2DMask, respectively. **b** DSC change analysis for PropSAM relative to MedSAM across various box ratios. This plot displays DSC changes, where blue indicates PropSAM-2DBox and red denotes PropSAM-2DMask. Each point on the graph represents a different object, highlighting the model’s adaptability to varying box ratios. **c** DSC change analysis for PropSAM relative to MedSAM across various convex ratios. **d** DSC change analysis for PropSAM relative to MedSAM across various inverse rotational inertia (IRI). **e** Comparative visualization of segmentation results for a sample with a low box ratio. The black arrow indicates an irregular area.

view box prompt used in MedSAM and SegVol (Wilcoxon rank-sum test,  $P < 0.0001$ ), while reducing interaction time by about 37.8% and aligning closely with the practical needs of clinical practitioners. Besides, although one-view mask prompt (used in PropSAM-2DMask) requires more time than one-view box prompts, it offers a comparable interactive cost to the most common two-view box prompts ( $P = 0.2766$ ), and the detailed prompt information can greatly enhance the model’s overall performance (Figure 4a). These analyses demonstrate the advantages of PropSAM’s two types of prompts over the two-view box prompt, providing users with flexible options for practical application.

## 2.5 PropSAM exhibits predictive stability and consistency

As mentioned in Section 2.4, PropSAM operates with one-view prompts, typically selected by physicians according to response evaluation criteria in solid tumors (RECIST). To assess the impact of variations in prompts provided by different physicians on PropSAM’s performance, we conducted an ablation study. As depicted in Figure 4d–e, we simulated deviations from the RECIST-standard confirmed largest slice through five experimental groups, which included deviations of 0% (no deviation),  $\pm 5\%$ ,  $\pm 10\%$ ,  $\pm 15\%$ , and  $\pm 20\%$ . Both PropSAM-2DBox and PropSAM-2DMask demonstrated stable DSC across these variations, as confirmed by one-way ANOVA tests, with  $P$ -values of 0.6736 and 0.5985, respectively (see Supplementary Figure S9 and Supplementary Table S8 for further details). While performance slightly declined with increasing deviations, it is important to note that a deviation of  $\pm 20\%$ , which corresponds to a total range of 40%, is uncommon in clinical practice. Even with such substantial deviations, PropSAMs maintained commendable performance.

Moreover, during the inference process, PropSAMs iteratively selects the most marginal predicted slice as the next round’s guiding slice and guiding prompt. The distance of this slice from the original guiding slice could potentially affect the accuracy of subsequent predictions, particularly when far apart, as the propagation relationship weakens with distance. This influence may be amplified through iterative propagation, impacting the overall 3D segmentation of the object. To evaluate the impact of propagation slice thickness, we conducted another ablation study with propagation thicknesses of 10 mm, 20 mm, 30 mm, and 40 mm. As shown in Figure 4f–g, PropSAMs maintained predictive stability and consistency across these different thicknesses, as assessed by one-way ANOVA tests with  $P$ -values of 0.7114 and 0.6131, respectively (refer to Supplementary Figure S10 and Supplementary Table S9 for more details). Based on these findings, we empirically selected 20 mm as the default propagation thickness for PropSAMs.

In summary, through ablation experiments involving varied prompt deviations and propagation thicknesses, PropSAMs have demonstrated notable predictive stability and consistency. This provides a reliable foundation for the clinical application of PropSAMs.

## 2.6 PropSAM’s superior efficacy in segmenting complex and irregular objects

We visualized the qualitative segmentation results of different models as shown in Figure 5a. Our proposed PropSAMs effectively utilize propagation information between slices, resulting in visually complete and smooth segmentation outcomes. In contrast, MedSAM, which employs a ‘slice-by-slice prediction’ and merging strategy, and SegVol, which uses ‘patch-

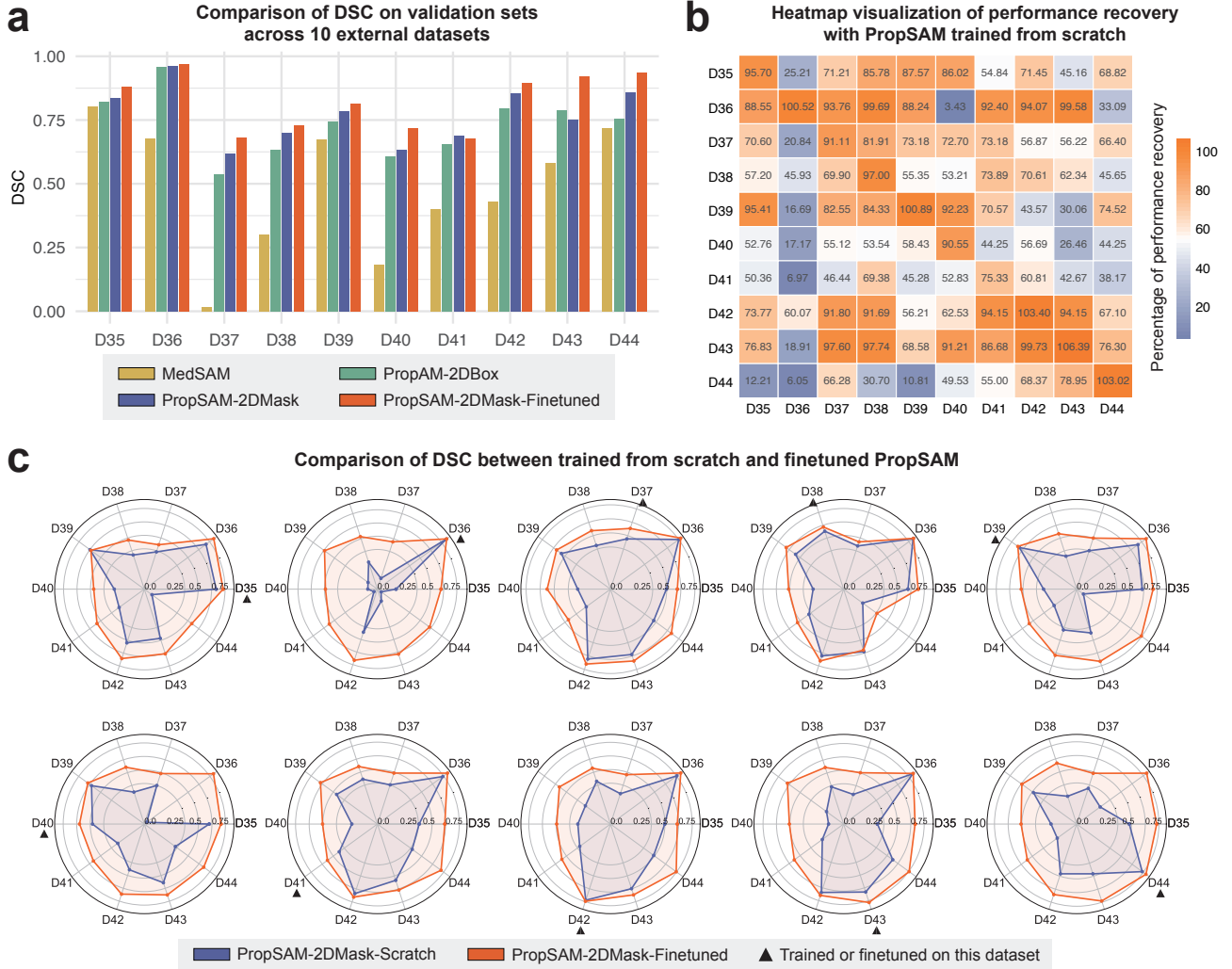


**Figure 6: Generalization analysis of PropSAM across multiple datasets.** **a** Bar chart visualization of DSC across external datasets. This bar chart compares the DSC performance of four models on validation sets from ten external datasets. The models compared include MedSAM in yellow, PropSAM-2DBox in green, PropSAM-2DMask in blue, and PropSAM-2DMask finetuned on corresponding datasets in red. The horizontal axis labels datasets D35 to D44, and the vertical axis represents the DSC performance. **b** Heatmap of performance recovery. The heatmap displays the percentage of performance recovery for PropSAM trained from scratch across ten datasets (each column) compared to the original trained PropSAM. Red indicates a recovery of more than 50%, with deeper reds showing higher percentages. Blue indicates recoveries below 50%, with deeper blues denoting lower percentages. **c** Radar chart comparison of DSC between trained from scratch and finetuned PropSAM. This radar chart visualizes the DSC comparison between PropSAM trained from scratch and finetuned on original trained PropSAM across datasets D35 to D44. Blue lines represent PropSAM trained from scratch, while red indicated finetuned PropSAM. Triangular markers point to the datasets used for training or finetuning.

by-patch prediction’ and then integrated them, do not achieve segmentation visualizations as refined as those produced by PropSAMs.

Moreover, we observed that the segmentation difficulty varies among different objects. For instance, most organs have relatively fixed shapes, making them easier to learn and segment, whereas some tissues or lesion-related objects present greater challenges. To quantify this process, inspired by BiomedParse [37], we evaluated the ‘irregularity’ of the objects and the accuracy of our predictions for these irregular objects through the following metrics:

1. Box ratio: evaluates the similarity between the target mask and its tight bounding box, denoted as  $BoxRatio(M) = \frac{|M|}{|Box(M)|}$ , where  $Box(M)$  is the tightest bounding box around mask  $M$ , and  $|\cdot|$  represents the area measured in pixels.
2. Convex ratio: measures how convex the target mask is, defined as  $ConvexRatio(M) = \frac{|M|}{|ConvexHull(M)|}$ , where  $ConvexHull(M)$  is the convex hull of mask  $M$ .
3. Inverse rotational inertia (IRI): measures how spread out the area of the target mask is, expressed as  $IRI(M) = \frac{0.75|M|}{(0.8\pi RI(M))^{\frac{5}{3}}}$ , where the rotational inertia of  $M$  relative to its centroid  $c_M$  is  $RI(M) = \sum_{x \in M} \|x - c_M\|_2^2$ , where  $x$  is the coordinate of each pixel in the mask, with  $c_M$  being the centroid coordinate.

As demonstrated in Figure 5b–d, PropSAM shows performance improvements over MedSAM across most segmentation objects (DSC change  $> 0$ ). Furthermore, these improvements are more pronounced when the three irregularity metrics are smaller ( $r < -0.1249$ ), indicating that PropSAM is particularly effective at handling irregular objects and is a more accurate reflection of real-world challenges. Additionally, we visualized the segmentation results for four models on a sample with a box ratio of 0.281 in Figure 5e. It is clear that the qualitative results of PropSAM are closest to the ground truth. This is notable especially since the segmentation object in this sample, unlike a typical kidney, includes a tumor, resulting in an irregularly indented shape indicated by the black arrow. PropSAM successfully identifies this unique feature, whereas MedSAM and SegVol struggle to accurately discern this specific part. This success also underscores that PropSAM’s learning focus is more robust, enabling it to dynamically adapt to rare and complex shape variations based on changes in structure and semantics between slices. In contrast, MedSAM and SegVol may find these abnormalities challenging due to their reliance on features typical of a normal kidney. These analyses demonstrate the potential of PropSAMs for precise segmentation of various objects, particularly those with irregular shapes.

## 2.7 PropSAM demonstrates strong generalization and adaptability across diverse segmentation tasks

We further explored PropSAM’s generalization capabilities from two perspectives: model fine-tuning and training from scratch. Firstly, as depicted in Figure 6a, PropSAM, serving as a general segmentation model, outperforms MedSAM on ten external datasets, demonstrating its robust generalization ability to unfamiliar datasets and objects. We then partitioned these ten datasets into training and validation sets and conducted minimal fine-tuning of PropSAM on the training sets to create the PropSAM-2DMask-Finetuned model. Experiments indicate that with minimal data fine-tuning, PropSAMs can quickly adapt

to corresponding tasks and enhance performance. However, it is noteworthy that the improvement of PropSAM-2DMask-Finetuned over PropSAM-2DMask is less significant compared to PropSAM’s improvement over MedSAM (paired t-test,  $P = 0.0017$ ), suggesting that the general model of PropSAM already performs well on unseen objects.

Secondly, we trained PropSAM from scratch on the divided training set and evaluated the performance recovery percentage relative to the general model PropSAM across the ten datasets (as shown in Figure 6b). The experiments reveal that even with limited data, training PropSAM from scratch can achieve over 75.33% performance recovery on corresponding datasets, indicating that PropSAM’s learning tasks are sufficiently straightforward to allow rapid adaptation on limited samples. Furthermore, we observed that segmentation objects with similar structures to the training objects benefited in performance. For instance, when trained from scratch on dataset D35, the performance recovery on D39 reached 87.57% due to the objects in these two datasets are both lesion-related and structurally similar. This further underscores that PropSAM’s learning focus is not specific semantic objects, but rather the structural or semantic information transfer relationships between slices.

Additionally, using radar charts (Figure 6c), we showcased the segmentation performance on ten datasets using the general model fine-tuned (PropSAM-2DMask-Finetuned) and trained from scratch (PropSAM-2DMask-Scratch). As noted, aside from performing well on the datasets where it was fine-tuned, PropSAM-2DMask-Scratch also achieved commendable performance on datasets with similar structural segmentation objects. Generally, the performance of PropSAM-2DMask-Finetuned is superior to PropSAM-2DMask-Scratch, indicating that on one hand, the general capabilities aid in fine-tuning specific objects and achieving more precise segmentation results [38, 39], and on the other hand, it demonstrates PropSAM’s adequate general capability to handle various segmentation objects.

These analysis highlight PropSAM’s robust generalization capabilities, showcasing its effectiveness in both fine-tuned and from-scratch training scenarios across diverse datasets and structural variations, affirming its adaptability and precision in segmentation tasks.

### 3 Discussion

Volumetric segmentation plays a pivotal role in medical imaging, serving essential downstream tasks such as disease diagnosis, surgical planning, and therapy monitoring. Traditional approaches typically involve extensive manual annotation by experts to train specialized segmentation models for specific medical scenarios. This process is costly, inefficient, and struggles to adapt to the expanding scale of clinical demands. With the advent of large model technologies, particularly the emergence of SAM, there is hope for achieving general segmentation capabilities. These models, trained on large-scale data, exhibit robust segmentation with minimal human interaction and maintain impressive generalization, especially for unseen objects. Such capabilities perfectly align with clinical needs, potentially accelerating the delineation process, rapidly accumulating high-quality annotated data, and enhancing the stability of downstream analysis tasks.

Current general segmentation models primarily draw from the success of SAM in natural image processing, categorized into two types based on basic model architecture and inference strategy differences. The first type (type I models) adapts SAM’s 2D model architecture directly to medical images through extensive training or fine-tuning in medical images, exem-

plifying initial exploration into general segmentation models in medical tasks. However, these models, by using ‘slice-by-slice prediction’, overlook the 3D spatial continuity present in medical images, which is crucial in volumetric segmentation, resulting in performance with room for improvement. The second type (type II models) extends the SAM architecture to 3D, incorporating more comprehensive 3D spatial continuity but at the cost of notably increased parameters. These models still underperform due to the limited medical volumetric annotation datasets available that are insufficient to fully leverage their capabilities. Furthermore, their computational cost is compounded by the necessity to predict and merge 3D overlap-stride patches individually.

Recognizing the challenges of these existing models, we propose a new approach leveraging the continuous nature of information between slices in 3D medical images—PropSAM (type III model). PropSAM combines a 2D CNN-based UNet architecture for intra-slice information learning and precise segmentation with a Transformer-based attention module for inter-slice information propagation and prompt-guided fusion. PropSAM consistently outperforms earlier models in terms of performance across multiple medical modalities and segmented objects and exhibits stability across variations in prompts and different parameter settings, particularly showing robust generalization on external datasets. Moreover, PropSAM delivers superior visualization results, especially adept at handling irregular objects, highlighting its advantages in segmentation precision and generalization. Thanks to the synergistic design of PropSAM’s CNN-based and Transformer-based modules, along with its overall 2D model architecture, it achieves highly efficient inference speeds. Unlike previous methods, PropSAM’s inference can propagate bilaterally from the initial guiding slice, leveraging inter-slice information propagation without the need for overlapping stride inference and object merging. Additionally, compared to purely Transformer-based architectures like MedSAM and SegVol, PropSAM effectively employs a CNN-based part for local medical feature-depiction—crucial for precise medical object segmentation—while using a minimal Transformer-based part for necessary long-distance inter-slice relational building. This design not only reduces the overall parameter count but also tailors user interaction to clinical needs by requiring only one-view prompts, contrasting the two-view interactions needed for existing models.

Another notable distinction of PropSAM from existing methods is its learning focus. While the existing models learn to segment specific objects (e.g., given a prompt for liver, they segment the liver), PropSAM adopts a different approach by learning the propagation relationship of an object across slices, essentially discarding the concept of specific objects and instead learning structural or semantic continuity. On the one hand, this learning focus allows more training objects to be derived. For example, for an object with ten slices, we can form dozens of training tasks by specifying different guiding slices and extracting different adjacent slices. On the other hand, learning propagation information between slices enables the model to learn a more generalizable structural or semantic propagation relationship, displaying promising generalization capabilities as evidenced by high performance across external datasets and unseen objects.

Furthermore, PropSAM can be also viewed as an autoregressive model. Autoregressive models, particularly the generative pre-trained transformer (GPT) series [40, 41, 42, 43], have made advanced strides in various fields by utilizing a ‘predict next token’ approach. This method allows them to accumulate comprehensive knowledge from vast datasets and effectively function as a hybrid of thousands of distinct multi-tasks, thereby enhancing the models’ ability to learn and generalize knowledge [41, 44]. PropSAM employs a guiding slice and prompt to ‘predict the next slice,’ using the resulting predictions to

iteratively continue the process. During training, PropSAM constructs a guiding slice and prompt together with its adjacent slices as a task. This strategy mirrors the approach of the GPT model by generating thousands of diverse propagation multi-tasks, which not only assists the model in learning general propagation relationships but also enhances its potential for generalizability compared to other models that operate under a 'prompt to segment specific objects' framework. Additionally, this indicates that PropSAM could benefit from the advanced technologies of existing successful autoregressive models, potentially further showcasing its capability in the segmentation of generic medical 3D objects.

Despite the promising success of the current version of PropSAM, it still faces two limitations: 1) Although extensive experiments have proven PropSAM's segmentation efficacy and generalization, as well as its efficiency and cost-effectiveness, segmentation tasks are merely an intermediate step in clinical practice that serve various downstream tasks. Therefore, we plan to integrate PropSAM into clinical settings as software or a web application, combining it with patient diagnostics and prognosis to study its practical clinical implications in the future; 2) Currently, while PropSAM supports the most common prompt forms used by physicians, 2D bounding boxes and 2D sketch masks, there's room to incorporate more interactive forms such as dotting or drawing lines. We aim to further enhance PropSAM to build a more comprehensive system and product.

In summary, this study introduces PropSAM, a new propagation-based general segmentation method to segment any 3D objects across various modalities for medical images. PropSAM demonstrates exceptional segmentation capabilities and strong generalization abilities across 44 datasets and multiple medical modalities, alongside higher inference and interaction efficiencies. Sufficient experiments indicate its potential application in clinical practice, poised to become an effective assistant for physicians and other users.

## 4 Methods

### 4.1 Data acquisition

We collected 44 public 3D medical segmentation datasets(see Supplementary Table S1) covering multiple modalities, such as CT, MR, PET-CT and micro-CT, to build a large-scale and comprehensive dataset for model training and validating(Figure 1a). Since those datasets we collected have been widely used as the training and validating data of universal and specialized medical images segmentation models, all the volumetric medical images present in our dataset possess high-quality annotations.

As Supplementary Table S4 and Figure 3b illustrated, we recorded these 44 in five dimensions: number of 3D scans, number of voxels, size anisotropy, spacing anisotropy, and variety of object types, which are essential for a comprehensive evaluation of PropSAMs. Following nnUNet [1], size anisotropy is defined as the ratio of the smallest to the largest size in 3D scans and spacing anisotropy is calculated as the ratio of the smallest to the largest spacing in 3D scans. Furthermore, in alignment with the protocol established in MedSAM [13], we partitioned these datasets into 34 internal datasets (D01–D34) for training and validation, and ten external datasets (D35–D44) for independent testing (Supplementary Tables S2–S3).

As Supplementary Table S2 and S4 shown, our dataset contains 168 different categories of objects and 1,645,871 3D



objects, covering organs, lesions and issues, for experiment analysis to enhance the stability and generalization capability of the two main modules Box2Seg module and PropSAMs.

## 4.2 Data pre-processing

Firstly, to obtain bounding boxes for Box2Mask module, we generated a tightest bounding box on the slice where the corresponding foreground mask annotation contains over 100 pixels. Then we randomly adjusted the width and height of the bounding box with a scaling ratio between 1.0 to 1.25 to account for potential deviation in actual usage and used the processed bounding box as training data for Box2Mask module. Correspondingly, we constructed ROI tasks for PropSAM. We generated the tightest bounding box around the mask of the guiding slice and then randomly adjusted its width and height with a scaling ratio between 1.0 to 2.0 to capture the context around the target object. This adjusted bounding box was then used to crop both the guiding slice and the adjacent slices sampled within the propagation thickness, forming the cropped ROI tasks as training data for PropMask module.

The training data for both Box2Seg and PropSAM requires two steps of data pre-processing: images normalization and enhancement by random data augmentation. After acquiring the ROI images/tasks, we applied normalization to clip the intensity values to the range between the 0.5th and 99.5th percentiles of pixel values within the annotated mask of the original slice images, which represent the minimum and maximum values, respectively. The context of foreground ROI images/tasks were enhanced and emphasized after normalization. Finally, to optimize training efficiency, we applied offline data augmentation five times for each sample for Box2Mask module. Specifically, each image had a 50% chance of being flipped horizontally and vertically. Additionally, we randomly adjusted the image’s brightness and contrast, also with a 50% probability, setting the adjustment ranges to  $[-0.2, 0.2]$ . The images were also rotated randomly up to 45 degrees with a 50% probability, filling any areas outside the original boundaries with a constant value (typically black). Otherwise, since the fundamental training unit of PropMask is a task, each containing several images (typically 20 adjacent images and one guiding image). Specifically, each image in a task had a 50% chance of being flipped horizontally or vertically and being rotated up to 45 degrees. These samples were uniformly resized to a resolution of 224 for input into the Box2Mask module and PropMask module.

Following these pre-processing steps, we obtained a total of 19,344,368 samples for Box2Mask module and 1,345,871 tasks across 43 datasets comprising 284 objects (Figure ??a). According to the data partitioning in MedSAM, these data were divided into internal and external validation datasets. The internal validation dataset was further split into training and validation sets at an 80:20 ratio. There were 14,974,620 training samples, 3,782,206 internal validation samples, and 587,542 external validation samples for Box2Mask module (Supplementary Table S2) and 1,020,576 training samples, 258,889 interval validation tasks, and 66,406 external validation tasks for PropMask module (Supplementary Table S3). We trained PropSAM on the training set, with the internal validation set used to evaluate model performance and select the final model checkpoint. The external validation dataset served to demonstrate the robustness of PropSAM and its zero-shot capability with unseen objects and datasets.

### 4.3 Network architecture

PropSAM is composed of the Box2Mask module and the PropMask module. Both are built based on convolutional neural network (CNN), which have been the predominant network architecture in the field of computer vision for a long time and are more efficient compared to the commonly used Transformer architecture nowadays, making them suitable for a broader range of clinical application settings. And we note that the UNet-based architecture[16], particularly the nnUNet model[1], has become the most widely adapted and effective approach for medical imaging segmentation in recent years.

To convert ROI images, which are cropped according to bounding box prompts, to binary foreground masks (Figure 2a), we employed a six-stage encoder-decoder UNet-based network[16] as the Box2Mask module. The input utilizes three-dimensional channels, appropriate for a grayscale image replicated three times. The initial stage features 32 channels, which doubles with each subsequent stage, capping at 512. Thus, the channel counts across the six stages are [32, 64, 128, 256, 512, 512]. Each stage includes two convolutional layers, followed by instance normalization[45] and the activate function LeakyReLU. All convolutional kernels are 3, with a stride of one within each stage and a stride of two in the last layer of each stage for down-sampling. Additionally, to maintain low-frequency features, skip connections were employed to bridge each encoder level with its corresponding decoder. We also produced binary foreground segmentation predictions at all six decoding stages for deep supervision.

We obtained a 2D mask from two styles of prompts via Box2Mask module. The 2D mask serves as the segmentation for the initial guiding slice, and the PropMask module utilizes it to generate segmentation for the adjacent slices by propagating the segmentation of the guiding slice (Figure 2b). As the core component of the network and its architecture is largely based on UNet[16]. PropMask consists of an image encoder, a mask encoder, a sequence of cross-attention modules and a decoder. The image encoder and mask encoder are also six-stage CNN encoders, which are the same as the encoder of Box2Mask module, but the input channel of the mask encoder is one to accept the 2D mask prompt directly. Both the guiding slice and its adjacent slices go through the image encoder to produce support features and query features of six resolution ( $[224 \times 224, 112 \times 112, 56 \times 56, 28 \times 28, 14 \times 14, 7 \times 7]$ ), respectively. Similarly, the 2D mask from the guiding slice go through the mask encoder to produce mask features of six resolutions. Subsequently, a sequence of cross-attention modules are employed. Given a set of query vectors  $Q$ , key vectors  $K$ , and value vectors  $V$ , the definition of cross-attention is as follows:

$$\text{Attention}(Q, K, V) = \text{Softmax}\left(\frac{QK^T}{\sqrt{d_k}}\right)V$$

where  $QK^T$  represent the dot product between queries and keys, which measures the similarity or alignment between the queries and keys and cross-attention is particularly used when the sets of queries, keys and values are derived from different input sources, enabling the model to integrate information across the sources.

Support features, query features and mask features of PropMask are respectively flattened into 1-dimensional vectors, serving as the support, query and value vectors for cross-attention. Considering the definition of cross-attention, the outputs of the cross-attention modules of PropMask can be regarded as the value vectors for the query features. The output value

vectors can be reshaped to 2D feature maps, which serve as the feature maps for query images. To balance the model efficiency and performance, cross-attention modules are executed only on the lowest four resolution feature maps of the slice and mask ( $[56 \times 56, 28 \times 28, 14 \times 14, 7 \times 7]$ ). Finally, the output of cross-attention at the lowest resolution go through multiple de-convolutions in the decoder to generate outputs of varying resolutions, which match the shapes of image features of the six-stage encoder. Following the skip connection structure of the UNet architecture[16], the output from each stage of the decoder is concatenated with the feature maps of the same resolution from either the cross-attention module or the encoder stage to be the input of the next decoder stage and the final output of the decoder is the prediction mask, which is used to calculate dice loss with ground truth mask label for backpropagation.

#### 4.4 Training configuration and inference settings

We utilized PyTorch[46](version 2.0.0) to implement our models and executed them on a server equipped with the CUDA platform(version 11.8). The Box2Mask module and the PropSAM module was trained using four NVIDIA A800-SXM4-80GB GPUs and 64 Intel(R) Xeon(R) Platinum 8358 P CPUs(2.60GHz). The AdamW optimizer was utilized with an initial learning rate of  $1e-3$  for Box2Mask module and  $5e-4$  for PropMask module as well as a weight decay of  $1e-4$ . The learning rate was adjusted according to Cosine Annealing LR schedule with a maximum period of 100 epochs and a minimum eta of  $1e-5$ .

For Box2Mask module, during each epoch, we randomly selected 10,000 samples for training and conducted evaluations every 20 epochs using a set of 5,000 randomly sampled validation samples. The training lasted for 4,100 epochs, with a batch size of 1,024, over a span of about six days. Supplementary Figure S5 illustrates the training and validation curves. We selected the latest checkpoint as the final weight configuration for our Box2Mask module. Once we trained the Box2Mask module, we salloc one GPU and 8 CPUs for inference evaluation, as well as the compared methods, to ensure that inference time and resource comparisons fair. For inference phase, we first cropped the ROI images from the promptable bounding boxes, then normalized them by a series of candidate minimum and maximum parameters. The minimum parameters are determined using the 5th to 40th percentiles (in steps of 1), while the maximum parameters are determined using the 90th to 95th percentiles (in steps of 0.5). These parameters are then combined to a standardize the ROI images, resulting in candidate normalized ROI images. Subsequently, the Box2Mask module is employed to predict the foreground. The final standardization parameters,  $v_{min}$  and  $v_{max}$ , are determined based on the 0.5th and 99.5th percentile values of the pixel locations predicted as foreground. These parameters are then used to standardize the ROI images prediction.

For PropMask module, throughout the training process, we randomly selected 10,000 tasks per epoch. Each task consists of the guiding slice and four randomly sampled adjacent slices. Evaluations were conducted every 20 epochs using a set of 5,000 randomly selected validation tasks. The training extended 4,500 epochs, with a batch size of 160, lasting approximately seven days. Supplementary Figure S8 displays the training and validation loss curves. We chose the most recent checkpoint as the final weight configuration for our PropMask module.

## 4.5 Loss function

The Box2Mask module leverages deep supervision, enabling predictions at six distinct stages, denoted as  $\{\mathbf{P}_1, \dots, \mathbf{P}_S\}_{S=6}$ . Each prediction,  $\mathbf{P}_s$ , activated by the Sigmoid function, outputs a 2D representation where values between  $[0.0, 1.0]$  indicate the probability that each pixel is part of the foreground. The foreground ground truth is accordingly rescaled to align with the resolutions of these six stages, represented as  $\{\mathbf{M}_1, \dots, \mathbf{M}_S\}_{S=6}$ , where each  $\mathbf{M}_s$  is binary with 1 indicating the foreground. To calculate the loss, we apply soft dice loss at each stage and then compute the average of these losses to derive the overall loss function, which is expressed as:

$$L_{\text{Box2Mask}} = \frac{1}{S} \sum_{s=1}^S \left( 1.0 - \frac{2 \times \sum_{i=1}^{W_s} \sum_{j=1}^{H_s} \mathbf{P}_{s,i,j} \mathbf{M}_{s,i,j}}{\sum_{i=1}^{W_s} \sum_{j=1}^{H_s} \mathbf{P}_{s,i,j}^2 + \sum_{i=1}^{W_s} \sum_{j=1}^{H_s} \mathbf{M}_{s,i,j}^2} \right), \quad (1)$$

where  $W_s$  and  $H_s$  denote the resolution at the  $s$ th stage. The loss ranges from 0.0 to 1.0, ensuring that the module is trained effectively across all resolutions, thus enhancing its predictive accuracy and reliability.

## 4.6 Evaluation metrics

We evaluated the model from two aspects. For segmentation performance evaluation, we used the Dice Similarity Coefficient (DSC) to evaluate the segmentation results. DSC is a set similarity metric commonly used to calculate the similarity between two samples, with a value range  $[0.0, 1.0]$ . The more accurate the segmentation result, the larger the DSC, and the closer it is to 1.

$$DSC = \frac{2|A \cap B|}{|A| + |B|} \quad (2)$$

where  $A$  represents the ground truth mask,  $B$  represents the predicted mask, and  $|\cdot|$  denotes the cardinality of a set (i.e., the number of elements in the set).

For efficiency evaluation, we used the inference time by recording the time from reading samples to writing final segmentation results. The lower the inference time, the more efficient the model is.

## 4.7 Statistics and reproducibility

Sample sizes and the number of datasets were determined based on the availability of all publicly available datasets that we could download and process, as well as a sparse modality dataset (D44) from our clinical practice (micro-CT). No statistical method was used to pre-determine the sample sizes or the number of datasets. DSC calculations were performed for every object type in all datasets, with the DSC of a dataset obtained by averaging the DSCs of its constituent objects. Performance comparisons across multiple experimental groups in ablation studies were conducted using a one-way ANOVA test; in this study, a  $P$ -value greater than 0.05 indicated no significant difference in performance across the groups, suggesting stability in the experimental results. Differences in inference speed and interaction time between models were assessed using the Wilcoxon rank-sum test; a  $P$ -value less than 0.05 indicated significant differences. And we used paired t-test to compare the

differences between the improvements between different models. The relationship between model performance improvements and object irregularity was modeled using a linear model, where a negative correlation coefficient ( $r$ ) indicates that greater irregularity is associated with more pronounced model improvements.

We used R (version 4.1.3) for results analysis and statistical analyses, and Python (version 3.7.10) for model construction, training, and inference. To ensure reproducibility, we have detailed our methodology in the supplementary materials, which include data collection and processing, module details, definitions of loss functions, experimental specifics, and evaluation metrics (Supplementary Figures S1–S10, Supplementary Tables S1–S10, and Supplementary Text S1). These procedures adhered to good clinical practice and data privacy regulations.

## Data availability statements

All datasets referenced in this study, except for dataset D44, are publicly available. Supplementary Table S1 provides the download links. The D44 dataset should be obtained by submitting a reasonable request to the corresponding author. The source code and supporting materials are available on GitHub<sup>3</sup>. All R packages employed in this study can be found on CRAN<sup>4</sup> or <sup>5</sup>.

---

<sup>3</sup><https://github.com/czifan/PropSAM>

<sup>4</sup>[https://cran.r-project.org/web/packages/available\\_packages\\_by\\_name.html](https://cran.r-project.org/web/packages/available_packages_by_name.html)

<sup>5</sup>Bioconductor (<https://www.bioconductor.org/>)

## References

- [1] Isensee, F., Jaeger, P. F., Kohl, S. A., Petersen, J. & Maier-Hein, K. H. nnu-net: a self-configuring method for deep learning-based biomedical image segmentation. *Nature methods* **18**, 203–211 (2021).
- [2] De Fauw, J. *et al.* Clinically applicable deep learning for diagnosis and referral in retinal disease. *Nature medicine* **24**, 1342–1350 (2018).
- [3] Yuan, M. *et al.* Devil is in the queries: advancing mask transformers for real-world medical image segmentation and out-of-distribution localization. In *Proceedings of the IEEE/CVF Conference on Computer Vision and Pattern Recognition*, 23879–23889 (2023).
- [4] Cao, K. *et al.* Large-scale pancreatic cancer detection via non-contrast ct and deep learning. *Nature medicine* **29**, 3033–3043 (2023).
- [5] Ferrari, V. *et al.* Value of multidetector computed tomography image segmentation for preoperative planning in general surgery. *Surgical endoscopy* **26**, 616–626 (2012).
- [6] He, M. *et al.* Associations of subcutaneous fat area and systemic immune-inflammation index with survival in patients with advanced gastric cancer receiving dual pd-1 and her2 blockade. *Journal for Immunotherapy of Cancer* **11** (2023).
- [7] Ouyang, D. *et al.* Video-based ai for beat-to-beat assessment of cardiac function. *Nature* **580**, 252–256 (2020).
- [8] Li, J. *et al.* Ct-based delta radiomics in predicting the prognosis of stage iv gastric cancer to immune checkpoint inhibitors. *Frontiers in Oncology* **12**, 1059874 (2023).
- [9] He, M. *et al.* Deep learning model based on multi-lesion and time series ct images for predicting the benefits from anti-her2 targeted therapy in stage iv gastric cancer. *Insights into Imaging* **15**, 1–14 (2024).
- [10] Zaidi, H. & El Naqa, I. Pet-guided delineation of radiation therapy treatment volumes: a survey of image segmentation techniques. *European journal of nuclear medicine and molecular imaging* **37**, 2165–2187 (2010).
- [11] Bao, P., Wang, G., Yang, R. & Dong, B. Deep reinforcement learning for beam angle optimization of intensity-modulated radiation therapy. *arXiv preprint arXiv:2303.03812* (2023).
- [12] Lu, L., Dercle, L., Zhao, B. & Schwartz, L. H. Deep learning for the prediction of early on-treatment response in metastatic colorectal cancer from serial medical imaging. *Nature communications* **12**, 6654 (2021).
- [13] Ma, J. *et al.* Segment anything in medical images. *Nature Communications* **15**, 654 (2024).
- [14] Wang, G. *et al.* Deepigeos: a deep interactive geodesic framework for medical image segmentation. *IEEE transactions on pattern analysis and machine intelligence* **41**, 1559–1572 (2018).

- [15] Wang, S. *et al.* Annotation-efficient deep learning for automatic medical image segmentation. *Nature communications* **12**, 5915 (2021).
- [16] Ronneberger, O., Fischer, P. & Brox, T. U-net: Convolutional networks for biomedical image segmentation. In *Medical image computing and computer-assisted intervention–MICCAI 2015: 18th international conference, Munich, Germany, October 5-9, 2015, proceedings, part III* 18, 234–241 (Springer, 2015).
- [17] Dorent, R. *et al.* Crossmoda 2021 challenge: Benchmark of cross-modality domain adaptation techniques for vestibular schwannoma and cochlea segmentation. *Medical Image Analysis* **83**, 102628 (2023).
- [18] Tang, X. *et al.* Whole liver segmentation based on deep learning and manual adjustment for clinical use in sirt. *European journal of nuclear medicine and molecular imaging* **47**, 2742–2752 (2020).
- [19] Primakov, S. P. *et al.* Automated detection and segmentation of non-small cell lung cancer computed tomography images. *Nature communications* **13**, 3423 (2022).
- [20] Xie, W., Jacobs, C., Charbonnier, J.-P. & Van Ginneken, B. Relational modeling for robust and efficient pulmonary lobe segmentation in ct scans. *IEEE transactions on medical imaging* **39**, 2664–2675 (2020).
- [21] Soomro, T. A. *et al.* Image segmentation for mr brain tumor detection using machine learning: a review. *IEEE Reviews in Biomedical Engineering* **16**, 70–90 (2022).
- [22] Antonelli, M. *et al.* The medical segmentation decathlon. *Nature communications* **13**, 4128 (2022).
- [23] Kirillov, A. *et al.* Segment anything. In *Proceedings of the IEEE/CVF International Conference on Computer Vision*, 4015–4026 (2023).
- [24] Ravi, N. *et al.* Sam 2: Segment anything in images and videos. *arXiv preprint arXiv:2408.00714* (2024).
- [25] Du, Y., Bai, F., Huang, T. & Zhao, B. Segvol: Universal and interactive volumetric medical image segmentation. *arXiv preprint arXiv:2311.13385* (2023).
- [26] Huang, Y. *et al.* Segment anything model for medical images? *Medical Image Analysis* **92**, 103061 (2024).
- [27] Mazurowski, M. A. *et al.* Segment anything model for medical image analysis: an experimental study. *Medical Image Analysis* **89**, 102918 (2023).
- [28] Deng, R. & Cui, C. Segment anything model (sam) for digital pathology: Assess zero-shot segmentation on whole slide imaging. *Medical Imaging with Deep Learning (MIDL)* (2023).
- [29] Hu, C., Xia, T., Ju, S. & Li, X. When sam meets medical images: An investigation of segment anything model (sam) on multi-phase liver tumor segmentation. *arXiv preprint arXiv:2304.08506* (2023).

- [30] He, S., Bao, R., Li, J., Grant, P. E. & Ou, Y. Accuracy of segment-anything model (sam) in medical image segmentation tasks. *arXiv preprint arXiv:2304.09324* (2023).
- [31] Wald, T. *et al.* Sam. md: Zero-shot medical image segmentation capabilities of the segment anything model. In *Medical Imaging with Deep Learning, short paper track* (2023).
- [32] Zhou, T., Zhang, Y., Zhou, Y., Wu, Y. & Gong, C. Can sam segment polyps? *arXiv preprint arXiv:2304.07583* (2023).
- [33] Wu, J. *et al.* Medical sam adapter: Adapting segment anything model for medical image segmentation. *arXiv preprint arXiv:2304.12620* (2023).
- [34] Cheng, J. *et al.* Sam-med2d. *arXiv preprint arXiv:2308.16184* (2023).
- [35] Zhu, J., Qi, Y. & Wu, J. Medical sam 2: Segment medical images as video via segment anything model 2. *arXiv preprint arXiv:2408.00874* (2024).
- [36] Subakan, C., Ravanelli, M., Cornell, S., Bronzi, M. & Zhong, J. Attention is all you need in speech separation. In *ICASSP 2021 - 2021 IEEE International Conference on Acoustics, Speech and Signal Processing (ICASSP)*, 21–25 (2021).
- [37] Zhao, T. *et al.* Biomedparse: a biomedical foundation model for image parsing of everything everywhere all at once (2024). URL <https://arxiv.org/abs/2405.12971>. 2405.12971.
- [38] Xie, W., Willems, N., Patil, S., Li, Y. & Kumar, M. Sam fewshot finetuning for anatomical segmentation in medical images. In *Proceedings of the IEEE/CVF Winter Conference on Applications of Computer Vision*, 3253–3261 (2024).
- [39] Li, Y., Hu, M. & Yang, X. Polyp-sam: Transfer sam for polyp segmentation. In *Medical Imaging 2024: Computer-Aided Diagnosis*, vol. 12927, 759–765 (SPIE, 2024).
- [40] Radford, A. Improving language understanding by generative pre-training (2018).
- [41] Radford, A. *et al.* Language models are unsupervised multitask learners. *OpenAI blog* **1**, 9 (2019).
- [42] Brown, T. B. Language models are few-shot learners. *arXiv preprint ArXiv:2005.14165* (2020).
- [43] Achiam, J. *et al.* Gpt-4 technical report. *arXiv preprint arXiv:2303.08774* (2023).
- [44] Sanh, V. *et al.* Multitask prompted training enables zero-shot task generalization. *arXiv preprint arXiv:2110.08207* (2021).
- [45] Ulyanov, D., Vedaldi, A. & Lempitsky, V. Instance normalization: The missing ingredient for fast stylization. *arXiv preprint arXiv:1607.08022* (2016).
- [46] Paszke, A. *et al.* Pytorch: An imperative style, high-performance deep learning library. *Advances in neural information processing systems* **32** (2019).